Modelling of the fatigue cracking resistance of grid reinforced asphalt concrete by coupling fast BEM and FEM

Anicet Dansou, Saida Mouhoubi, Cyrille Chazallon, Marc Bonnet

Modelling of the fatigue cracking resistance of grid reinforced asphalt concrete by coupling fast BEM and FEM

A. Dansou[a,b] , S. Mouhoubi[a], C. Chazallon[a] and M. Bonnet[c]

[a]ICube, UMR 7357, CNRS, Université de Strasbourg
INSA de Strasbourg, 24 bd de la victoire, 67084 Strasbourg Cedex, France

[b]LTDS, UMR 5513, CNRS, Université de Lyon
ECL ENISE, 58 Rue Jean Parot, 42023 Saint-Etienne Cedex 2, France

[c]POEMS, UMR 7231, CNRS, ENSTA, INRIA
ENSTA Paris, 91762 Palaiseau Cedex, France

ARTICLE HISTORY
Compiled January 13, 2022

ABSTRACT
We present a computational modeling approach aimed at investigating the effect of fiber grid reinforcement on crack opening displacement and fatigue crack propagation. Grid reinforcements are modeled using elastic membrane finite elements, while the cracked concrete is treated using a symmetric boundary element method (BEM), which in particular allows easy geometrical modelling and meshing of cracks. The BEM is accelerated by the fast multipole method, allowing the handling of potentially large BEM models entailed by three-dimensional configurations hosting multiple cracks. Fatigue crack growth is modelled using the Paris law. The proposed computational approach is first verified on a reinforced cracked beam, and then applied to a three-dimensional configuration featuring a grid-reinforced asphalt pavement.

KEYWORDS
Grid reinforcement; Crack propagation; Surface-breaking crack; Galerkin BEM; Fast Multipole Method

1. Introduction

Fiber grid reinforcements are used since a few decades ago to delay the development of fatigue cracking in asphalt concrete pavements. However, the behavior of reinforced structures is still not fully understood, and design methods are mainly based on experience. Many experimental studies have been conducted to evaluate the cracking resistance of reinforced structures. They include standard laboratory tests on samples performed on three point bending tests (3PB) or four point bending tests (4PB) or slab bending, combined with monotonic loading or fatigue loading, see Canestrari, Belogi, Ferrotti, and Graziani (2013); Khodaii, Fallah, and Moghadas Nejad (2009); Millien, Dragomir, Wendling, Petit, and Iliescu (2012); Safavizadeh, Wargo, Guddati, and Kim (2015); Zofka, Maliszewski, and Maliszewska (2017); Arsenie, Chazallon, Duchez, and Hornych (2017); Tam, Park, Le, and Kim (2020). For full scale tests on pavements, see

CONTACT A. Dansou. Email: anicet.dansou@enise.ec-lyon.fr

Hornych et al. (2012) or Chen, Hanandeh, Abu-Farsakh, and Mohammad (2018). An interesting review on glass fiber grids used for pavement reinforcement is presented by M.-L. Nguyen, Blanc, Kerzrého, and Hornych (2013). A practical design method is recently presented in Zofka and Maliszewski (2019).

The study of grid performance by numerical modeling can be divided into three parts. First, there are simplified models, developed by companies and universities, based on empirical data and numerical simulation results to evaluate reinforced structures performance, for example BITUFOR by Vanelstraete, Leonard, and Veys (2000), OLCRACK/THERMCR by Thom (2000) or ARCDESO by Bondt, Schrader, Bijsterveld, and Long (2005). Secondly, there are several numerical models for replicating laboratory experiments which consist of studying the grid effect on samples, see Bacchi (2009), Arsenie, Chazallon, Duchez, and Mouhoubi (2017) or Sagnol, Quezada, Chazallon, and Stockner (2019). Thirdly, there is the simulation of the grid effect on the reinforced structure. There are few studies in this part and most of them use two-dimensional finite element analysis or axial symmetric analysis, see Abu-Farsakh, Gu, Voyiadjis, and Chen (2014); Gu, Luo, Luo, Hajj, and Lytton (2017); M. L. Nguyen et al. (2020); Taherkhani and Jalali (2017); Tang, Stoffels, and Palomino (2016). For 3D simulation, non-local approaches are often applied. Coni and Bianco (2000) investigated crack propagation process in presence of steel reinforcement based on FEM using ANSYS. Baek and Al-Qadi (2009) used FEM to investigate the fracture behavior of hot-mix asphalt (HMA) overlays with a bilinear cohesive zone model.

However, the finite element method requires a high degree of refinement around the crack front for stress and displacement fields to be computed accurately, which hampers its efficiency for the study of fatigue cracking in 3D configurations. Moreover, each stage of simulated propagation entails local re-meshing near the new crack front, which is quite cumbersome. The eXtended Finite Element Method (XFEM), developed by Belytschko and Black (1999), Moës, Dolbow, and Belytschko (1999), Fries and Belytschko (2010) and Belytschko, Liu, Moran, and Elkhodary (2014), is more efficient than the classical FEM for fracture problems, see Oliver, Huespe, and Sánchez (2006); Sukumar, Chopp, Béchet, and Moës (2008), due to its ability to model the crack and its evolution without remeshing. Alternatively, the boundary element method constitutes a powerful alternative to FEM, particularly in cases where better accuracy is required due to stress concentration in problems such as crack propagation simulation. The most important feature of BEMs is that the solution is approximated on the boundaries, while equilibrium and compatibility are exactly satisfied in the domain. Hence, for 3D problems, only the boundary surface needs meshing, see Fig. 1, which greatly facilitates remeshings associated with crack advancement. Equipping BEMs with advanced acceleration techniques, such as the Fast Multipole Method (FMM),

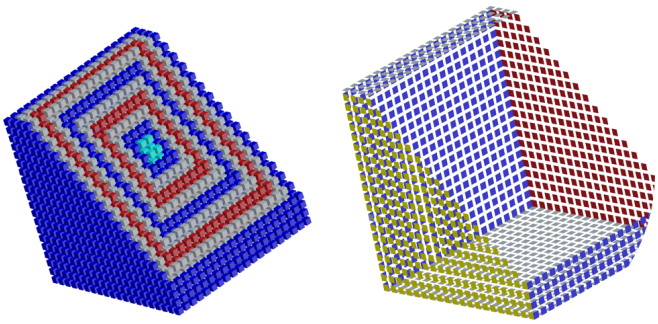

Figure 1. A 3D mesh: FEM (left); BEM (right)

for faster computation greatly enhances the performance of large-scale BEM analyses, see e.g. Greengard and Rokhlin (1987); Yoshida (2001); Trinh, Mouhoubi, Chazallon, and Bonnet (2015), and many other references therein.

In this work, a new computational approach, based on the coupling of finite element method and fast multipole boundary element method, is developed to evaluate the fatigue cracking resistance of fiber grid reinforced structures, and implemented in an in-house code named MBEMv3.1. We first present the multipole boundary element method formulation, the simulation of crack propagation and the incorporation of grid reinforcement in structures through an approximate elastic membrane model. Then, the fiber grid effect is studied for a reinforced beam containing an internal crack or a surface-breaking crack. Finally, the fatique cracking resistance is studied on a 3D configuration, namely a grid-reinforced asphalt concrete pavement.

2. Fast Multipole Symmetric Galerkin BEM

2.1. Symmetric Galerkin BEM

In this work, we employ the symmetric Galerkin version of the BEM (SGBEM). This version is based on a variational framework and produces a symmetric coefficient matrix, a feature that, among other advantages, facilitates BEM/FEM coupling, see e.g. Costabel (1987); Ganguly, Layton, and Balakrishna (2000) or Springhetti, Novati, and Margonari (2006).

Let us consider a fractured elastic solid Ω subjected to prescribed tensions $\boldsymbol{t}^D$ on the boundary S_t and displacement constraints $\boldsymbol{u}^D$ on S_u (Fig. 2). The boundary of Ω (including the crack S_c) is thus defined as $S = S_t \cup S_u \cup S_c$. The crack surface S_c supports a displacement discontinuity $\boldsymbol{\phi}$, usually referred to as the crack opening displacement (COD) and defined in (1) as

$$\boldsymbol{\phi}(\boldsymbol{x}) = \boldsymbol{u}(\boldsymbol{x}^+) - \boldsymbol{u}(\boldsymbol{x}^-), \tag{1}$$

where $\boldsymbol{u}^+(\boldsymbol{x})$ and $\boldsymbol{u}^-(\boldsymbol{x})$ are the traces of $\boldsymbol{u}$ on the upper and lower sides of S_c (the unit normal to S_c pointing by convention from the lower to the upper side). Details of the mathematical developments of the SGBEM can be found in many references, e.g. Bonnet (1999). The variational boundary integral formulation for the cracked

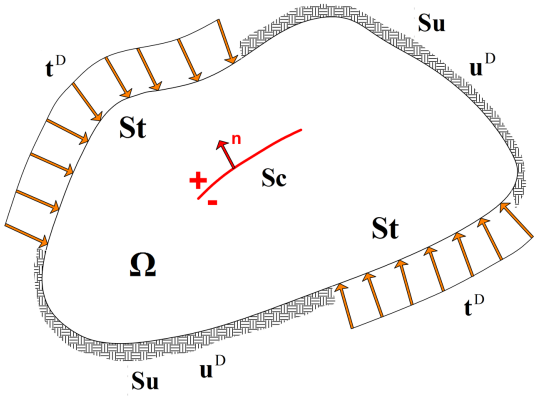

Figure 2. Solid containing a crack: notation

elastic solid is written as: find $\boldsymbol{u} \in \mathcal{V}_u,\ \boldsymbol{\phi} \in \mathcal{V}_c,\ \boldsymbol{t} \in \mathcal{V}_t$ such that

$$\left.\begin{aligned} \mathcal{B}_{uu}(\boldsymbol{u},\widetilde{\boldsymbol{u}}) + \mathcal{B}_{tu}(\boldsymbol{t},\widetilde{\boldsymbol{u}}) + \mathcal{B}_{cu}(\boldsymbol{\phi},\widetilde{\boldsymbol{u}}) &= \mathcal{F}_u(\widetilde{\boldsymbol{u}}) \\ \mathcal{B}_{ut}(\boldsymbol{u},\widetilde{\boldsymbol{t}}) + \mathcal{B}_{tt}(\boldsymbol{t},\widetilde{\boldsymbol{t}}) + \mathcal{B}_{ct}(\boldsymbol{\phi},\widetilde{\boldsymbol{t}}) &= \mathcal{F}_t(\widetilde{\boldsymbol{t}}) \\ \mathcal{B}_{uc}(\boldsymbol{u},\widetilde{\boldsymbol{\phi}}) + \mathcal{B}_{tc}(\boldsymbol{t},\widetilde{\boldsymbol{\phi}}) + \mathcal{B}_{cc}(\boldsymbol{\phi},\widetilde{\boldsymbol{\phi}}) &= \mathcal{F}_c(\widetilde{\boldsymbol{\phi}}) \end{aligned}\right\} \quad \text{for all } \widetilde{\boldsymbol{u}} \in \mathcal{V}_u, \widetilde{\boldsymbol{\phi}} \in \mathcal{V}_c, \widetilde{\boldsymbol{t}} \in \mathcal{V}_t \tag{2}$$

The bilinear forms $\mathcal{B}_{uu}$ etc. and linear functionals $\mathcal{F}_u$ are usual integral operators written in weak form. Their explicit expressions are provided in Pham, Mouhoubi, Chazallon, and Bonnet (2012). For example, we have

$$\begin{aligned} \mathcal{B}_{tt}(\boldsymbol{t},\widetilde{\boldsymbol{t}}) &= \int_{S_u}\int_{S_u} t_k(\boldsymbol{x}) U_i^k(\boldsymbol{x},\widetilde{\boldsymbol{x}}) \tilde{t}_i(\widetilde{\boldsymbol{x}}) dS_{\tilde{x}}\, \mathrm{d}S_x \\ \mathcal{B}_{tu}(\boldsymbol{t},\widetilde{\boldsymbol{u}}) &= -\int_{S_u}\int_{S_T} t_k(\boldsymbol{x}) T_i^k(\boldsymbol{x},\widetilde{\boldsymbol{x}}) \tilde{u}_i(\widetilde{\boldsymbol{x}}) dS_{\tilde{x}}\, \mathrm{d}S_x \\ \mathcal{B}_{\phi\phi}(\boldsymbol{\phi},\widetilde{\boldsymbol{\phi}}) &= \int_{S_c}\int_{S_c} [R\phi]_{iq}(\boldsymbol{x}) B_{ikqs}(\boldsymbol{r}) [R\tilde{\phi}]_{ks}(\widetilde{\boldsymbol{x}})\, \mathrm{d}S_{\tilde{x}} dS_x \end{aligned} \tag{3}$$

where the unknowns $\boldsymbol{u}, \boldsymbol{t}$ and $\boldsymbol{\phi}$ have respective supports S_t, S_u and S_c; $U_i^k(\boldsymbol{x},\widetilde{\boldsymbol{x}})$ and $T_i^k(\boldsymbol{x},\widetilde{\boldsymbol{x}})$ are the i^{th} component of the Kelvin fundamental displacement and traction, respectively, at $\boldsymbol{x} \in \mathbb{R}^3$ created by a point force applied at $\widetilde{\boldsymbol{x}} \in \mathbb{R}^3$ along the k^{th} coordinate direction, given by (4)

$$\begin{aligned} U_i^k(\boldsymbol{x},\widetilde{\boldsymbol{x}}) &= \frac{1}{16\pi\mu(1-\nu)r}[\hat{r}_i\hat{r}_k(3-4\nu) + \delta_{ik}] \\ T_i^k(\boldsymbol{x},\widetilde{\boldsymbol{x}}) &= -\frac{1}{8\pi(1-\nu)r^2} n_j(\boldsymbol{x})[3\hat{r}_i\hat{r}_k\hat{r}_j + (1-2\nu)(\delta_{ik}\hat{r}_j + \delta_{jk}\hat{r}_i - \delta_{ij}\hat{r}_k)] \end{aligned} \tag{4}$$

having set $\boldsymbol{r} = \boldsymbol{x} - \widetilde{\boldsymbol{x}},\ r = \|\boldsymbol{r}\|,\ \hat{\boldsymbol{r}} = \boldsymbol{r}/r$, with δ_{ij} denoting the Kronecker symbol, μ the shear modulus and ν the Poisson ratio. The bilinear forms ((3)) are all defined in terms of $O(r^{-1})$ weakly singular kernels, following a preliminary regularization based on the Stokes theorem together and indirect regularization, see Li, Mear, and Xiao (1998). The surface curl operator R arises as a result of this manipulation and is defined by (5):

$$[Ru]_{ks}(\widetilde{\boldsymbol{x}}) = e_{jfs} n_j \partial_f u_k(\widetilde{\boldsymbol{x}}) \tag{5}$$

(with $e_{jfs} = 1$ if (j,f,s) is a circular permutation of $(1,2,3)$ and -1 otherwise, implicit sommation over repeated indices being assumed) while the weakly singular fourth-order tensor $\boldsymbol{B}$ is given in component form by (6)

$$B_{ikqs}(\boldsymbol{r}) = \frac{1}{8\pi(1-\nu)r}[2\delta_{qs}\hat{r}_i\hat{r}_k + 2(\delta_{ik}\delta_{qs} - 2\nu\delta_{is}\delta_{kq} - (1-\nu)\delta_{iq}\delta_{ks})] \tag{6}$$

The function spaces in problem (2), which are the same for the unknowns $\boldsymbol{u}$, $\boldsymbol{\phi}$, $\boldsymbol{t}$ and the associated test functions $\widetilde{\boldsymbol{u}}$, $\widetilde{\boldsymbol{\phi}}$, $\widetilde{\boldsymbol{t}}$ are rigorously defined in many references, e.g. Costabel and Stephan (1987). To implement Galerkin discretizations of problem (2), natural finite-dimensional subspaces of $\mathcal{V}_u, \mathcal{V}_c$ are provided by continuous interpolations of $\boldsymbol{u}$ over S_t and $\boldsymbol{\phi}$ over S_c (with a zero trace on the edges ∂S_t, ∂S_c), while piecewise-continuous interpolation of $\boldsymbol{t}$ over S_u is sufficient for defining appropriate subspaces of $\mathcal{V}_t$. The SGBEM can therefore approximate all integral operators with

standard boundary element interpolations, whereas collocation methods for cracks put more severe constraints on the discretization options. The system of discretized equations arising from (2) is symmetric, and has the form

$$\mathbf{K}.\mathbf{X} = \mathbf{F} \tag{7}$$

where $\mathbf{X} \in \mathbb{R}^N$ collects all unknown degrees of freedom (DOFs) on S_t, S_c and S_u while the matrix $\mathbf{K} \in \mathbb{R}^{N\times N}_{\text{sym}}$ and the vector $\mathbf{F} \in \mathbb{R}^N$ result from discretizing the bilinear forms and the linear functionals, respectively, of the entering problem (2). All these features make SGBEM superior to the collocation approach. The matrix $\mathbf{K}$ is, however, fully populated (albeit symmetric), which places a practical limit of $N = O(10^4)$ on the size of SGBEM models solvable on ordinary computers, the computing work and memory required both becoming excessive otherwise.

2.2. Fast multipole method

The fast multipole method (FMM), introduced in Greengard and Rokhlin (1987), aims at improving the performance of boundary element analyses by circumventing the need to evaluate the kernel functions anew for each pair of boundary points encountered. This is achieved by introducing poles $\boldsymbol{x}_0, \widetilde{\boldsymbol{x}}_0$ (Fig. 3) at which contributions of clusters of points are gathered. The FMM rests on (i) decomposing the relative position vector $\boldsymbol{r} := \boldsymbol{x} - \widetilde{\boldsymbol{x}}$ as $\boldsymbol{r} = \boldsymbol{x}' + \boldsymbol{r}_0 - \widetilde{\boldsymbol{x}}'$ (Fig. 3) and (ii) reformulating the kernel functions as truncated series of products of functions of the local position vectors $\boldsymbol{x}', \widetilde{\boldsymbol{x}}'$. The cluster-wise treatment of contributions to integral operators is only valid for well-separated clusters. This motivates a recursive definition of such clusters using an octree-based partition of the space (smaller but nearer clusters becoming eligible to multipole expansions), which is the essence of the *multi-level* FMM used here. The multi-level elastostatic FMM enjoys as a result a $O(N)$ computational complexity. The FMM implicitly splits the SGBEM matrix $\mathbf{K}$ into $\mathbf{K} = \mathbf{K}_{\text{near}} + \mathbf{K}_{\text{FMM}}$, where $\mathbf{K}_{\text{FMM}}$ gathers the contributions arising from multipole expansions and $\mathbf{K}_{\text{near}}$ the close-range influence coefficients that have to be computed by traditional BEM quadrature (see Fig. 4 for a schematic description). The matrix $\mathbf{K}_{\text{FMM}}$ is of course not actually set up; rather, the FMM evaluates products $\mathbf{K}_{\text{FMM}}.\mathbf{X}$ that are used by an iterative solver (GMRES) applied to (7). Details of the FMM applied to elastostatic BIEs can be found in e.g. Yoshida (2001).

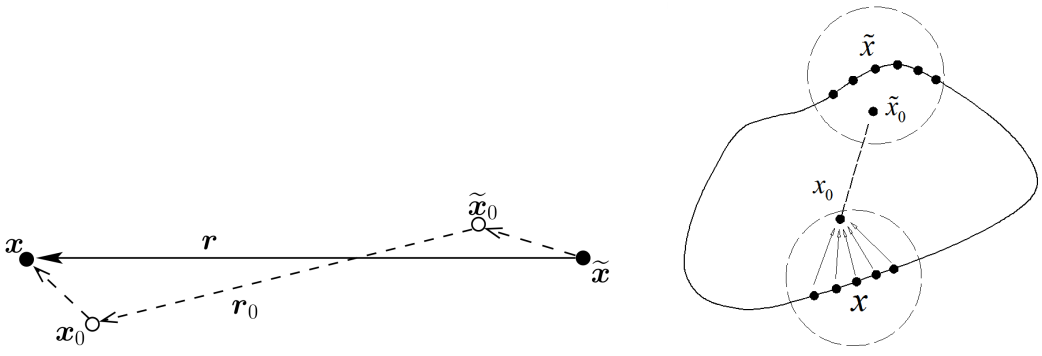

Figure 3. Decomposition of the position vector (left); Interactions by FMM scheme (right)

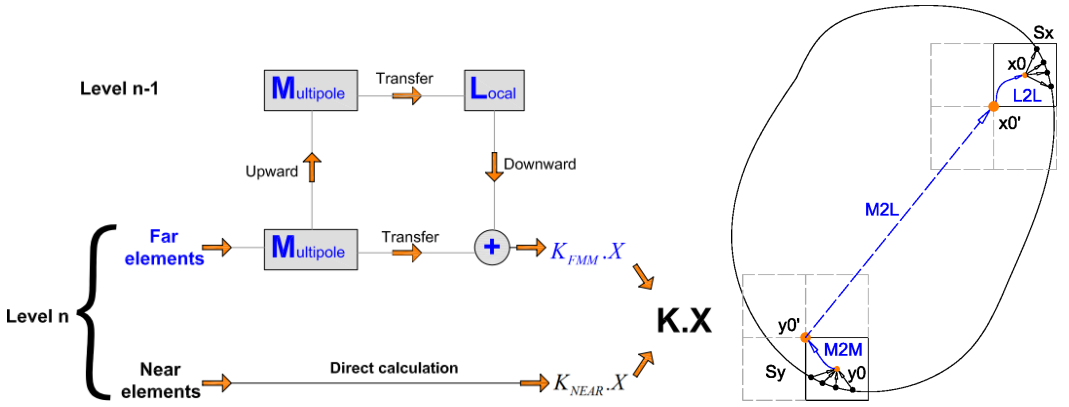

Figure 4. Two-level multipole algorithm (left); Multipole operations M2M, M2L and L2L (right)

3. Crack propagation simulation

3.1. MBEMv3.1

Based on SGBEM and FMM, Pham et al. (2012) and then Trinh et al. (2015) developed a Fortran code for 3D elasticity problems (MBEMv2.0). This software inherits a number of innovative features from the boundary element community such as: the singular integration schemes, the index of severity for adjusting the Gaussian quadrature density to the interelement distance, the nested Flexible GMRES (FGMRES) which uses the near-interaction matrix as a preconditioner and the extension to multizone configurations of the SGBEM. We have since developed a new version (MBEMv3.0) of this code, see Dansou, Mouhoubi, Chazallon, and Bonnet (2019) and Dansou, Mouhoubi, and Chazallon (2020). In this version, multiple strategies have been proposed and implemented for performance enhancement, including a data reusing technique, a shared memory parallelism using OpenMP directives and the proposal of a new sparse matrix method. The enhanced code has been run on various large-scale tests ($N = O(10^6)$) and has proved to be very robust and of excellent accuracy. The time speedup compared to MBEMv2.0 has exceeded 50 in some crack propagation simulations. For example, ten propagation cycles of 64 circular cracks in a cube sample are simulated in two hours on a 20-core computer. MBEMv3.0 can deal with surface-breaking cracks, complex multizone problems and proposed a direct coupling with FEM to simulate thin structures. However, previous versions did not include the simulation of crack propagation.

In this work, the coupling procedure is extended to crack propagation problems in complex configurations, where grid reinforcements are modelled as elastic membranes using the FEM while all surrounding media, which may contain multiple (and possibly surface-breaking) cracks, are modelled as 3D cracked elastic media using the accelerated BEM. The resulting new version of our code, named MBEMv3.1, is applied in this work to study the fatigue cracking resistance of grid reinforced asphalt concrete pavement containing surface-breaking cracks. Its main improvement, relative to earlier versions, hence lies in the simulation of surface-breaking crack propagation that takes into account a fiber grid.

All materials considered in MBEMv3.1 are assumed elastic isotropic. Important effects such as fracture strength effect or viscoelastic properties of asphalt material are therefore not taken into account in applications presented in sections 5 and 6.

The code considers crack opening displacement but do not consider crack closure effects. Using the BEM, closure effects can be solved as contact problem by applying an iterative process that determines determine the contact forces that prevent the COD to become negative, to be repeated until the COD is everywhere non-negative, see Holek and Fedeliński (2020). Since MBEMv3.1 is based on explicit modelling of cracks and the discontinuities of they support, several phenomena are not considered such as crack initiation and arbitrary crack nucleation. We finally mention that only circular and elliptical propagating cracks can for now be treated by MBEMv3.1 due to limitations of our current remeshing method.

3.2. SIF evaluation

Many investigations address the evaluation of SIFs, see for example Aliabadi, Rooke, and Cartwright (1987). The strain and elastic stress fields are singular along the crack front. We use the classical approach based on quarter-point elements along the crack front Barsoum (1976) in order to better capture the behavior near the crack front ∂S_c (see Fig. 5). The SIFs are hence evaluated through extrapolation from the displacement discontinuity field expressed in a local coordinate system $(\boldsymbol{\nu}(s), \boldsymbol{n}(s), \boldsymbol{t}(s))$ by (8a), (8b) and (8c) (see Bonnet (1999); Pham et al. (2012)).

$$K_{\mathrm{I}}^2 = \frac{\mu}{8(1-\nu)}\sqrt{\frac{2\pi}{a}}\left(4\boldsymbol{\phi}^5 - \boldsymbol{\phi}^1\right)\cdot\boldsymbol{n} \tag{8a}$$

$$K_{\mathrm{II}}^2 = \frac{\mu}{8(1-\nu)}\sqrt{\frac{2\pi}{a}}\left(4\boldsymbol{\phi}^5 - \boldsymbol{\phi}^1\right)\cdot\boldsymbol{\nu} \tag{8b}$$

$$K_{\mathrm{III}}^2 = \frac{\mu}{8}\sqrt{\frac{2\pi}{a}}\left(4\boldsymbol{\phi}^5 - \boldsymbol{\phi}^1\right)\cdot\boldsymbol{t} \tag{8c}$$

where K_{I}^2,K_{II}^2 and K_{III}^2 are respectively the mode I, II and III SIF at the node 2, $\boldsymbol{\phi}^1, \boldsymbol{\phi}^5$ are the nodal CODs at nodes 1 and 5, the nodes being numbered as shown in Fig. 5.

3.3. Propagation Criterion

Suitable criteria for crack propagation are still being debated, especially for 3D configurations. A simple criterion for fatigue crack growth is the Paris law, see Paris and Erdogan (1963). Many other propagation criteria are proposed, see e.g. Bouchard, Bay, and Chastel (2003); Ma (2005); Mi and Aliabadi (1994); Sun and Jin (2012) and Recho (2013). Paris postulated that sub-critical crack growth under fatigue loading can be predicted in terms of the ranges of stress intensity factors (SIFs) in the same way that thresholds on SIFs or energy release rate characterize brittle fracture. Abundant experimental evidence supports the view that the crack growth rate can be correlated with the cyclic variation in the SIFs, e.g. through

$$\frac{\mathrm{d}a}{\mathrm{d}N}(s) = A\Delta K^m(s) \tag{9}$$

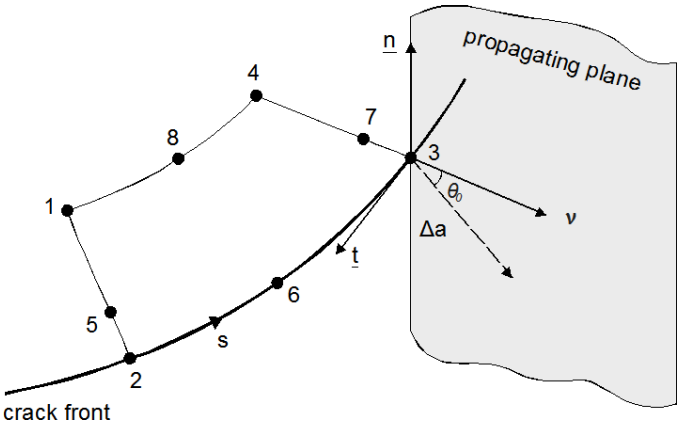

Figure 5. Quarter-point element along the crack front. Vectors $\boldsymbol{\nu}, \boldsymbol{n}, \boldsymbol{t}$ define a local coordinate frame at node **3**, their directions respectively correponding to the local opening, sliding and tearing modes of fracture.

where s is the arc length coordinate along the crack front, N is the current number of loading cycles, $\mathrm{d}a/\mathrm{d}N$ is the fatigue crack advancement rate per cycle, $\Delta K(s) = K^{\max}(s) - K^{\min}(s)$ is the SIF range for the current cycle, while A and m are parameters that depend on the material, environment, frequency, temperature and stress ratio.

The local configuration of the crack front described as in Fig. 5. The geometrical advance of the crack is described by moving points of the crack front in the local $(\boldsymbol{\nu}(s), \boldsymbol{n}(s))$ plane orthogonal to the front. The direction and length of the local crack advancement are represented respectively by the angle $\theta_0(s)$ and the step $\Delta a(s)$. The angle $\theta_0(s)$ is assumed to be given by the maximum circumferential stress criterion (Erdogan and Sih (1963); Frangi (2002)), see eq. (10)

$$\tan\frac{\theta_0}{2} = \frac{1}{4}\left(\frac{K_{\mathrm{Ieff}}}{K_{\mathrm{II}}} - \mathrm{sign}(K_{\mathrm{II}})\sqrt{\left(\frac{K_{\mathrm{Ieff}}}{K_{\mathrm{II}}}\right)^2 + 8}\right), \tag{10}$$

where $K_{\mathrm{Ieff}} = K_{\mathrm{I}} + B|K_{\mathrm{III}}|$ is an "effective" or "equivalent" local mode I stress intensity factor which accounts for the tearing mode being active ($K_{\mathrm{III}} \neq 0$), B being a material parameter. The local geometrical advancement Δa along $\cos\theta_0(s)\boldsymbol{\nu} + \sin\theta_0\boldsymbol{n}$ is determined from the Paris law (9) by (11):

$$\Delta a(s) = A\big(\Delta K_{\mathrm{I}}^2(s) + \Delta K_{\mathrm{II}}^2(s)\big)^{m/2}\Delta N. \tag{11}$$

If the computed crack increment $\Delta a(s)$ is too large, numerical inaccuracies will occur and significant re-meshing work will be needed. To avoid such situations, we fix *a priori* the maximum propagation length $\Delta a^{\max}$, find the node(s) where $\Delta K(s)$ is largest, evaluate the corresponding ΔN from (9) at that node, and then compute the extensions $\Delta a(s^i)$ by applying (9) at all crack front nodal positions s^i.

4. Grid reinforcement by FEM-BEM coupling

The symmetric Galerkin approach used in this work was proposed for FEM-BEM coupling to avoid the difficulties due to non-symmetric matrices, see Costabel (1987); Costabel and Stephan (1990). In recent works T. Nguyen, Rungamornrat, Senjuntichai, and Wijeyewickrema (2015) applied it for mode-I planar cracks simulation in elastic

media. Coupling approaches can be either FEM-driven or BEM-driven. In the former, the BEM subdomain is interpreted as a macro finite element that can be assembled easily to the FEM stiffness matrix Haas, Helldörfer, and Kuhn (2006); Mouhoubi (2000) and the global matrix equation is solved as a FE system. By contrast, the latter option, the FE subdomain contribution is incorporated into a boundary element system, see Brebbia and Georgiou (1979); Zienkiewicz, Kelly, and Bettess (1977). Other approaches are based on domain decomposition and iterative coupling, see for example Coulier, François, Lombaert, and Degrande (2014); von Estorff and Hagen (2005). Theoretical aspects of FEM-BEM coupling are surveyed in Gwinner and Stephan (2018).

In this work, the fiber grid reinforcement is modeled by membrane finite elements assumed homogeneous isotropic. A membrane is a medium treated as two-dimensional, the stresses being assumed to be constant along the thickness. It allows to model thin structures which have no flexural rigidity, or thick structures for which the stress tensor can be considered as constant through the thickness. The BEM-driven approach is adopted. The stiffness equations of the FEM, supported on the surfaces defining the membrane geometry, are coupled with the BEM and enforce continuity and equilibrium across the membranes. We adapt to membranes the symmetric BEM-FEM coupling procedure described in Margonari (2004); Springhetti et al. (2006). Let us consider the general coupling problem shown in Fig. 6. The Galerkin equations of the boundary element zone (zone A) can be written

$$\begin{bmatrix} B_{tt}^{AA} & B_{ut}^{AA} & B_{tt}^{IA} & B_{ut}^{IA} \\ B_{tu}^{AA} & B_{uu}^{AA} & B_{tu}^{IA} & B_{uu}^{IA} \\ B_{tt}^{AI} & B_{ut}^{AI} & B_{tt}^{II} & B_{ut}^{II} \\ B_{tu}^{AI} & B_{uu}^{AI} & B_{tu}^{II} & B_{uu}^{II} \end{bmatrix} \begin{Bmatrix} t^A \\ u^A \\ t^I \\ u^I \end{Bmatrix} = \begin{Bmatrix} \mathcal{F}_u(\tilde{t}^A) \\ \mathcal{F}_t(\tilde{u}^A) \\ \mathcal{F}_u(\tilde{t}^I) \\ \mathcal{F}_t(\tilde{u}^I) \end{Bmatrix} \tag{12}$$

The system of equations provided by the finite element method can be organized as

$$\begin{bmatrix} K^{II} & K^{IF} & M^I \\ K^{FI} & K^{FF} & 0 \end{bmatrix} \begin{Bmatrix} u^I \\ u^F \\ t^I \end{Bmatrix} = \begin{Bmatrix} F^I \\ F^F \end{Bmatrix} \tag{13}$$

where u^F is the unknown displacements of the finite element zone and matrix M^I represents the relationship between tractions and nodal forces on the interface I. Each

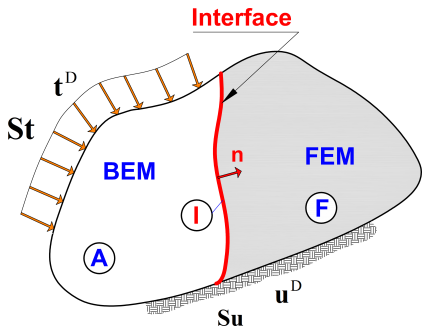

Figure 6. Generic BEM-FEM coupling problem: notation

term m that contributes to the construction of the matrix M^I has the form (14)

$$m = \int_I N^T N \, \mathrm{d}I \tag{14}$$

where N is the matrix of traditional shape functions. Equations (12) and (13) can be reorganized in the following system (15):

$$\begin{bmatrix} B_{tt}^{AA} & B_{ut}^{AA} & B_{tt}^{IA} & B_{ut}^{IA} & 0 \\ B_{tu}^{AA} & B_{uu}^{AA} & B_{tu}^{IA} & B_{uu}^{IA} & 0 \\ B_{tt}^{AI} & B_{ut}^{AI} & B_{tt}^{II} & B_{ut}^{II} & 0 \\ B_{tu}^{AI} & B_{uu}^{AI} & B_{tu}^{II} + M^I & B_{uu}^{II} + K^{II} & K^{IF} \\ 0 & 0 & 0 & K^{FI} & K^{FF} \end{bmatrix} \begin{Bmatrix} t^A \\ u^A \\ t^I \\ u^I \\ u^F \end{Bmatrix} = \begin{Bmatrix} \mathcal{F}_u(\tilde{t}^A) \\ \mathcal{F}_t(\tilde{u}^A) \\ \mathcal{F}_u(\tilde{t}^I) \\ \mathcal{F}_t(\tilde{u}^I) + F_I \\ F^F \end{Bmatrix} \tag{15}$$

The finite element stiffness matrix is then taken into account, when computing the global matrix-vector multiplication, during the iterative solution phase. In its present state, the proposed model assumes perfect anchoring of the reinforcement and does not take into account the possible rupture of the reinforcement layer (so does not model crack propagation through the reinforcement layer).

5. Numerical tests

This section reports numerical verification tests involving the bending of a (cracked and reinforced) beam. We consider a homogeneous beam ($E = 22\,\mathrm{MPa}$, $\nu = 0.3$) of dimensions $L = 6000\,\mathrm{mm}$, $b = 200\,\mathrm{mm}$ and $H = 500\,\mathrm{mm}$ clamped at both ends and subjected to a uniform pressure $q = 1$ MPa on its top face (Fig. 7a). The beam is meshed with 760 four-noded boundary elements and 762 nodes (Fig. 7b). In this section crack sizes are taken to facilitate numerical simulation.

5.1. Non-reinforced beam

As a preliminary verification, the computed deflection of the non-reinforced beam is computed and compared to finite element results obtained with Cast3m (Le Fichoux, 2011). The finite element mesh contains $40 \times 4 \times 5 = 800$ eight-noded cubic elements. The deflection comparison is presented in Fig. 8. The maximum vertical displacement obtained in the middle of the beam is $u_z = -15.1\,\mathrm{mm}$ with Cast3m FEM model and $u_z = -15.2\,\mathrm{mm}$ with our BEM code, which results in a relative difference of 0.66%.

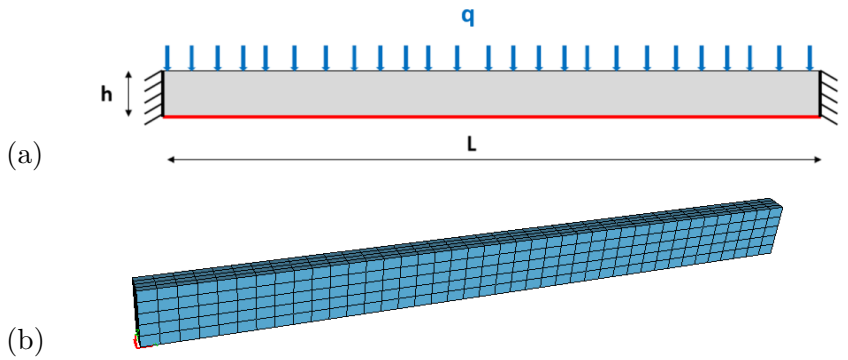

Figure 7. Beam example: (a) Geometry and loading, (b) BEM mesh

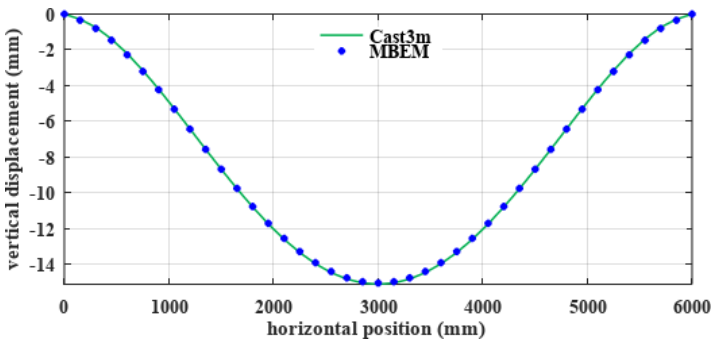

Figure 8. Non-reinforced beam: deflection verification

5.2. Fiber grid influence on deflection

This next simulation aims to verify the proposed FEM-BEM coupling involving a reinforcing membrane. We consider a grid reinforcement (thickness = 1 mm), perfectly bonded to the bottom of the beam. This reinforcement is taken homogeneous ($E_g = 200\,\text{GPa}$) and is modeled as a membrane using the FEM while the beam is still modeled by means of the BEM. The deflection of the reinforced beam is then computed and compared to finite element results obtained with Cast3m, see Fig. 9. The FEM model in Cast3m contains CUB8 elements for the beam and membrane elements for the reinforcement. This simulation verifies our FEM-BEM modeling of the reinforced structure, and additionally indicates that the deflection reduction due to the grid reinforcement is quite small (from $u_z^{\max} = -15.1\,\text{mm}$ to $u_z^{\max} = -14.5\,\text{mm}$).

5.3. Fiber grid influence on crack opening displacement

Let us consider now a vertical elliptic crack of dimensions $r_z = 50\,\text{mm}$, $r_y = 100\,\text{mm}$ and located 5 mm above the bottom face of the beam, see Fig. 10. The crack opening displacement is computed for the beam with and without reinforcement, at the center of the crack (according to y position) and by varying the vertical position (z), see in Fig. 11. The maximum crack opening displacement, obtained at the vertical position $z = 41\,\text{mm}$ is 0.192 mm (non-reinforced beam) or 0.177 mm (reinforced beam), so that the relative reduction on the maximum COD due to reinforcement is 8%.

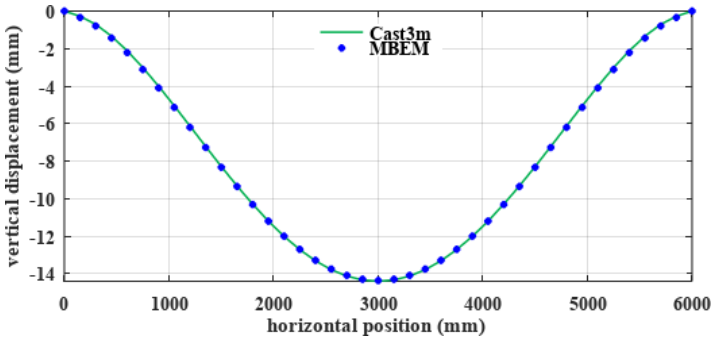

Figure 9. Reinforced beam: deflection verification

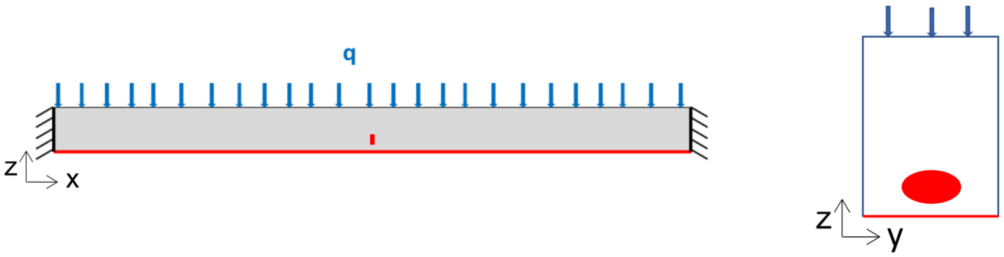

Figure 10. Cracked beam: geometry (left), middle cross-section with crack (right)

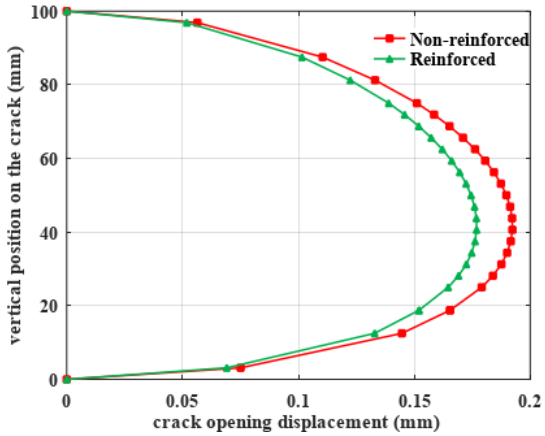

Figure 11. Reinforced beam: COD reduction at $y = 100mm$

5.4. Fiber grid influence on crack propagation

With the previous cracked beam (initially-elliptic crack with axes $r_z = 50\,\text{mm}$ and $r_y = 100\,\text{mm}$), we now simulate fatigue crack propagation by setting $A = 10^{-8}\,\text{mm/cycle}$ and $m = 4.5$ (Di Benedetto & Corté, 2004) in the Paris law (9). For this simulation, the crack is located 100 mm above the bottom face of the beam. The non-reinforced beam (model 1) is compared to reinforced beams with $E_g = 70\,\text{GPa}$ (model 2) and $E_g = 200\,\text{GPa}$ (model 3). The computed fatigue growth (vertical crack size r_z against number of loading cycles) is plotted for each of the three models in Fig. 12. The number of cycles required for the crack to reach $r_z = 150\,\text{mm}$ is 2.63×10^6 (model 1), 2.97×10^6 (model 2) or 3.68×10^6 (model 3), resulting in a performance improvement of 15% (model 2) or 45% (model 3).

5.5. Surface-breaking crack

Let us finally consider the influence of the grid reinforcement for surface-breaking cracks. We consider a semi-circular surface-breaking crack of radius $r_c = 25\,\text{mm}$ whose center is located at $x_c = 3000\,\text{mm}$, $y_c = 100\,\text{mm}$ and $z_c = 0\,\text{mm}$ (see Fig. 13). The non-reinforced beam (model 1) is compared to reinforced beams with $E_g = 20\,\text{GPa}$ (model 2) and $E_g = 70\,\text{GPa}$ (model 3). The crack does not break through the reinforcing membrane.

Fig. 14 presents this comparison for the crack opening displacement. The crack opening displacement at the middle of the crack-surface intersection ($x = 3000\,\text{mm}$,$y =$

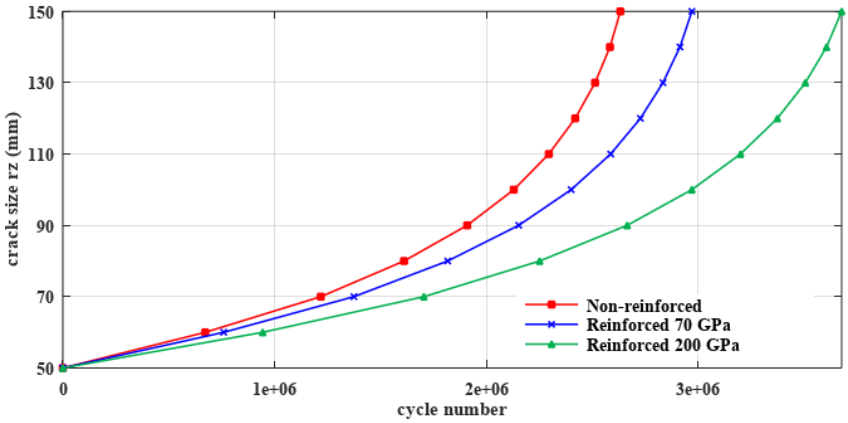

Figure 12. Reinforced beam: influence on propagation

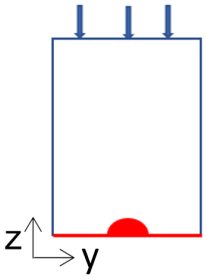

Figure 13. Beam with surface-breaking crack: yz plane

100 mm and $z = 0$ mm) is 112μm for the non-reinforced beam and 24μm for $E_g =$ 20 GPa and 13μm for $E_g = 70$ GPa. The relative difference on the COD due to the reinforcement is respectively 79% and 89%.

The computed fatigue growth (crack size r_y on crack-surface intersection against number of loading cycles) for the three models is plotted in Fig. 15. The number of cycles required for the crack to reach 75 mm in size is 2.0×10^6 for the non-reinforced beam 17×10^6 for $E_g = 20$ GPa and 40×10^6 for $E_g = 70$ GPa, which indicates a very significant performance improvement. The comparison between model 1 and model 2 permits to conclude that the cracking resistance of grid reinforcement results from the fact that the grid limits in-plane displacements (and hence the opening of surface-breaking cracks) rather than from using a grid material of high stiffness.

6. Application: reinforced road pavement

The work presented hereafter is a prospective study performed after the completion of the project SolDuGri (funded by the French National Research Agency), which dealt with the reinforcement of asphalt concrete pavements using glass fiber grids, where six different new pavement sections were tested simultaneously on the circular fatigue carousel (M. L. Nguyen et al., 2021). Here, we have used the mechanical characteristics of those materials, and we have considered cracks, and crack propagation criteria presented in section 5 of the present paper. Crack sizes are taken to facilitate numerical simulation. Then, we have modeled the pavement structures with a parametric study

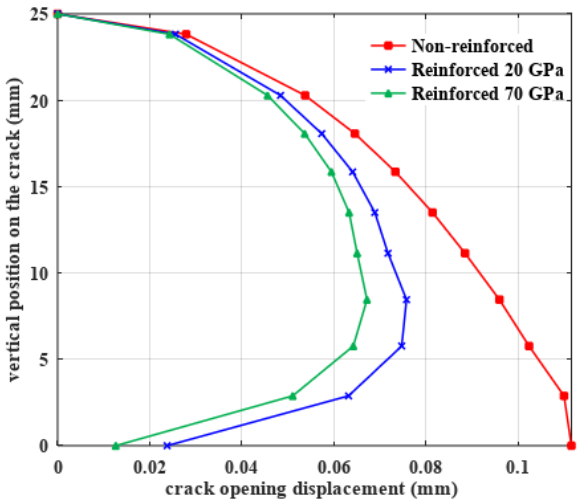

Figure 14. Grid influence on surface-breaking crack: COD at $y = 100mm$

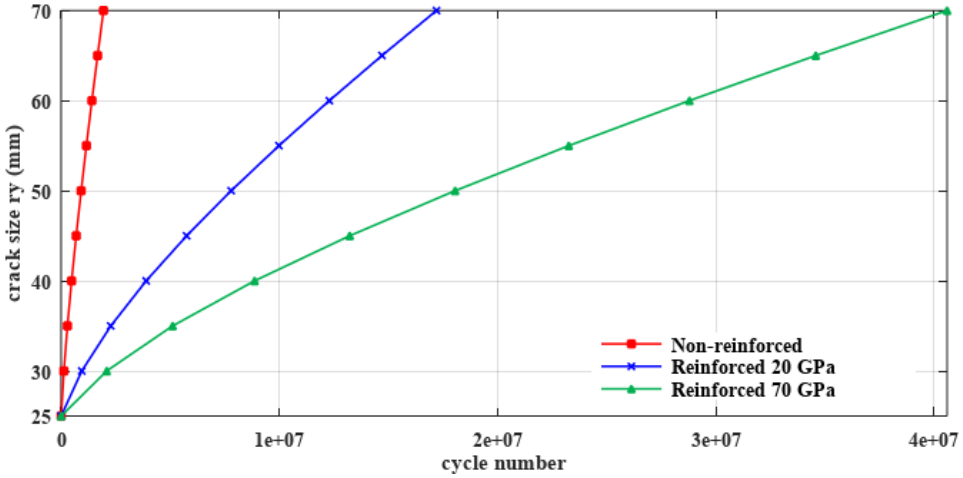

Figure 15. Grid influence on surface-breaking crack propagation

of grid stiffness but no comparison with the tested pavements have been carried out, because they were new (non-cracked) pavements.

In this example, we consider a portion of a three-layered heterogenous road of dimensions $3\,555{\times}3\,300{\times}2\,950\,\mathrm{mm}^3$, subjected to a wheel load of $p = 0.6\,\mathrm{MPa}$ at the top face (Fig. 16). The layer characteristics are given in Table 1. The road is meshed with 2 926 eight-noded boundary elements and 8 597 nodes. We then consider a semi-circular surface-breaking crack of radius $r_c = 25\,\mathrm{mm}$ embedded in the first layer and whose center is located at $x_c = 1777.5\,\mathrm{mm}$, $y_c = 1650\,\mathrm{mm}$ and $z_c = 2950\,\mathrm{mm}$ (see Fig. 16.b and Fig. 17). Fatigue crack propagation is simulated, with $A = 10^{-8}\,\mathrm{mm/cycle}$ and $m = 4.5$ (Di Benedetto & Corté, 2004) in the Paris law (9). We should mention that the wheel load is considered static, the position of the crack is such that only a radial propagation will be observed in the (x,z) plane and no bottom-up propagation is allowed.

The computed fatigue growth (crack size r_x on the crack-interface intersection against number of loading cycles) for this initial configuration (Fig. 18a) is plotted

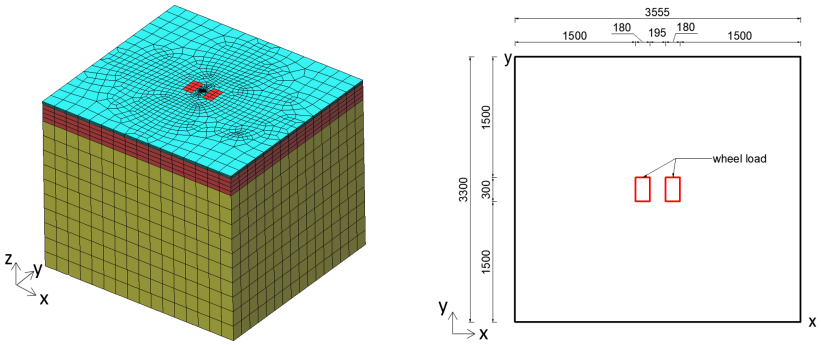

(a) Model (b) Geometry

Figure 16. Three-layered road

in Fig. 19, curve "Non-reinforced".

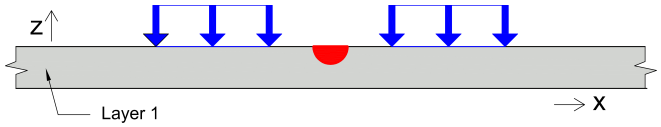

Figure 17. Crack position in first layer

The pavement is then reinforced with an asphalt concrete overlay of thickness 60 mm and with the same characteristics as the existing asphalt concrete layer (see Fig. 18b). The line labelled "+ Overlay60 " of Fig. 19 presents the fatigue growth (crack size r_x on the crack-interface intersection against number of loading cycles) for this configuration. As expected, the overlay reduces the propagation of the crack.

We have to mention here that the crack size is little (50 mm as diameter) and this leads to a large cycle number for double crack length.

In addition to the overlay we now add a fiberglass grid between the two asphalt concrete layers. This reinforcement will be modelled as a homogeneous membrane (thickness = 2 mm) and a parametric study of the stiffness has been carried out ranging from 3 GPa to 100 GPa. This membrane is located at position $z_g = 2950$ mm. We consider that there is no sliding between the membrane and the asphalt concrete layers (see Fig. 18c). The curve "+ Overlay60 + Grid 3 GPa" of Fig. 19 presents the fatigue growth for this configuration. The membrane finite elements used to model the grid limit the displacements in its (xy) plane due to their planar stiffness. Consequently, the crack propagation is also slowed down leading to the observed fatigue life improvement. The number of cycles required for the crack to reach a size $r_x = 50$ mm is 1.7×10^5 (non-reinforced pavement), 1.5×10^6 (pavement reinforced by an overlay) or 5.0×10^6 (pavement with overlay and fiberglass grid). Thus, the performance improvement factor is roughly 9 for the overlay reinforcement and 30 with the added fiberglass grid.

The fatigue growth for this last configuration is also computed by taking a high

Table 1. Three-layered road: layer characteristics

Layer	Layer constitution	Thickness (mm)	E (MPa)	ν
1	Asphalt concrete (BB)	50	11364	0,35
2	Granular base course (GNT)	300	400	0,35
3	Subgrade (Sol)	2600	200	0,35

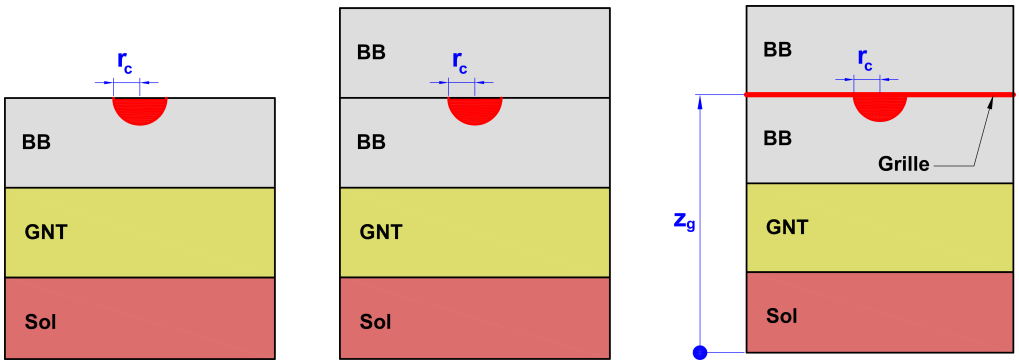

(a) Non-reinforced (b) + Overlay (c) + Overlay + Grid

Figure 18. Pavement layers: xz plane

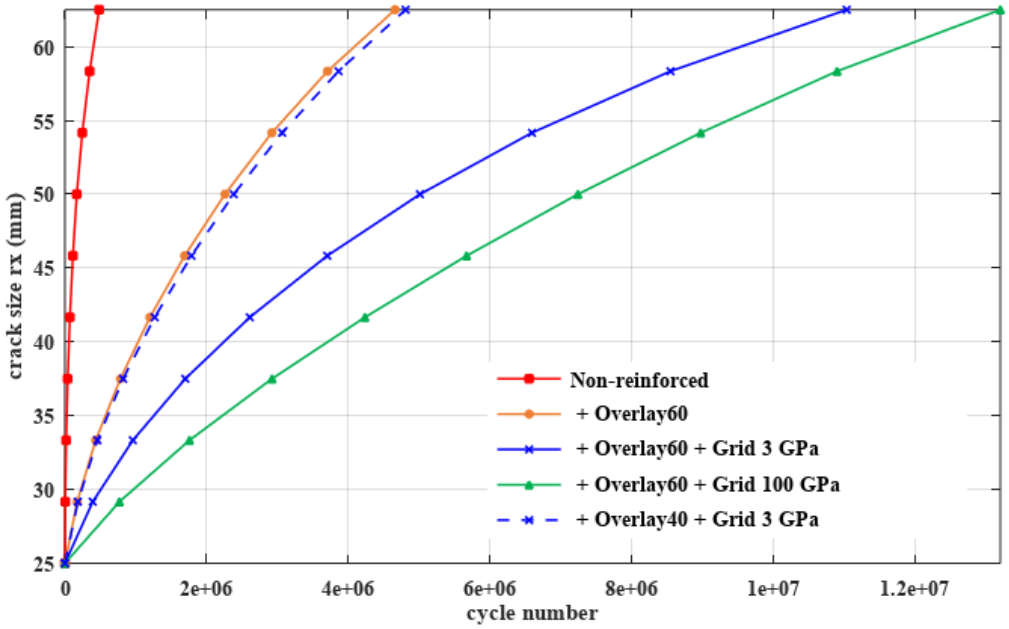

Figure 19. Cracking resistance of grid reinforced pavement (x direction)

grid Young's modulus $E_g = 100\,\text{GPa}$, see Fig. 19, curve "+ Overlay60 + Grid 100 GPa". The cycle number required to reach 50 mm is then 7.2×10^6 which corresponds to a performance improvement of 43. However, the performance improvement due to the modulus increasing (from $E_g = 3\,\text{GPa}$ to $E_g = 100\,\text{GPa}$) is only 1.4. This result shows that a too-rigid fiber is not necessary to improve the cracking resistance in the x direction.

Finally, we recall the reinforced model Fig. 18c ("+ Overlay60 + Grid 3 GPa") and then we reduce the thickness of the overlay from 60mm to 40mm. The curve "+ Overlay40 + Grid 3 GPa" presents the propagation results. This last curve is very close to the curve "+ Overlay60". The fatigue growth in z direction (crack size r_z) is presented in Fig. 20. One can observe that the light reinforcement (Grid 3GPa) with thin overlay (40 mm) does not prevent top-down crack propagation compared to non-reinforced case. What is observed also is that the "Overlay60" and stiff reinforcement (100GPa) do not improve the mechanical behaviour for crack propagation in the z

direction compared to "+ Overlay60". What can be concluded is that branching during crack propagation in (x,y) plane and propagation in the top direction are required to prevent this last effect, as it has been observed in some laboratory experiments.

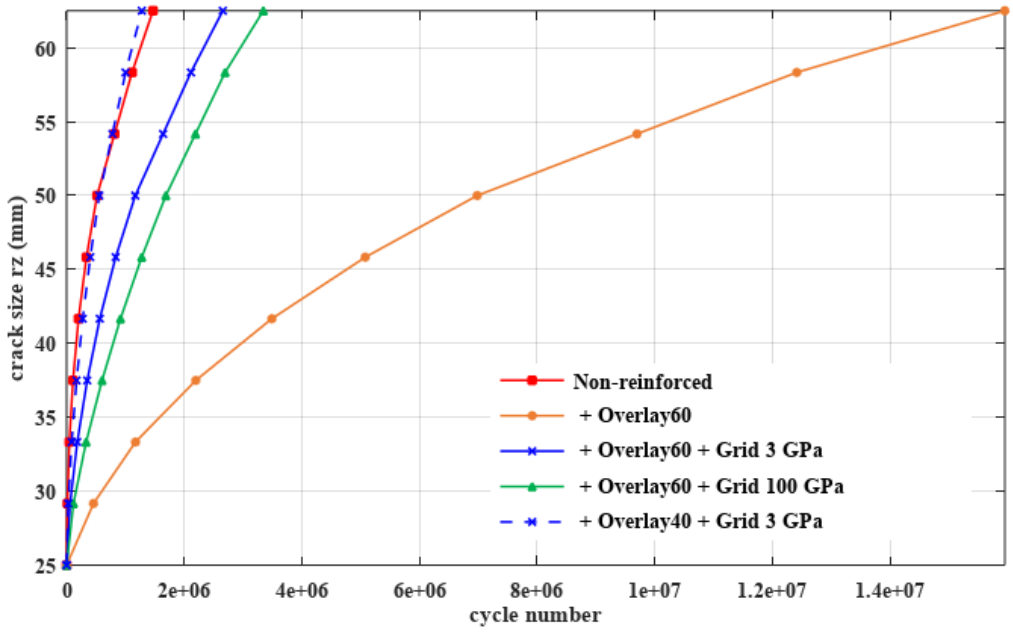

Figure 20. Cracking resistance of grid reinforced pavement (z direction)

The mapping of the number of cycles and crack propagation of all studied configurations when the crack size r_x reaches 50 mm are presented in Fig. 21 hereafter. We can clearly see the increase of crack size starting from a diameter of 50mm to 100 mm, and the shape of the crack for a given cycle number. The shape of the crack propagation is vertical because of the position of the initial crack and the fact that no wandering of the loading is applied.

The calculation for a pavement considering a damaged surface layer has been carried out with low elasticity modulus (half of the elasticity modulus : 5682MPa) and the overlay (11634 MPa) with and without a grid reinforcement or not. The results are presented in (Fig. 23 and Fig. 22). The same tendencies observed previously have been obtained.

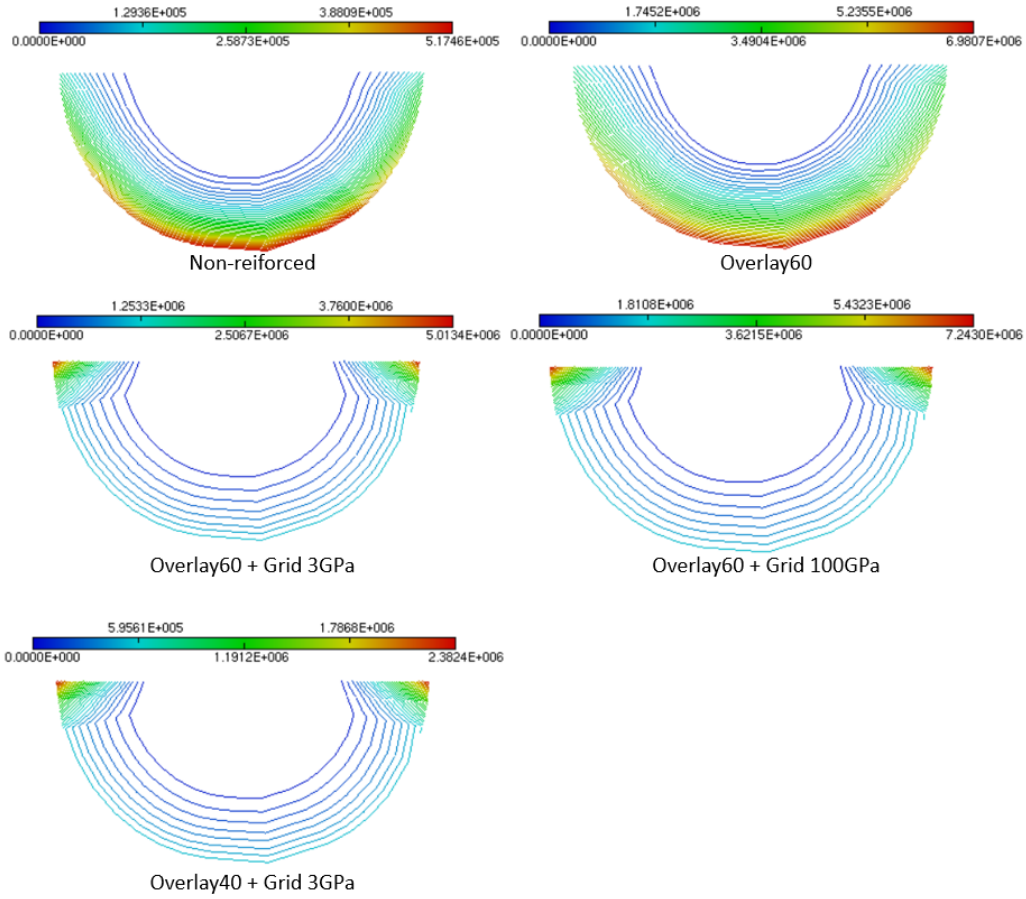

Figure 21. Cycle number mapping at from rx = rz = 25mm till rx = rz = 50 mm

7. Conclusion

In this research, the effect of fiber grid reinforcement on crack opening displacement and fatigue crack propagation is studied by using a robust numerical code based on the coupling of boundary element and finite element methods.

The main findings and conclusions of the study are as follows. Firstly, if we consider a double clamped bending beam:

- Fiber grid reinforcement has almost no effect on the deflection of reinforced structure in comparison with the non-reinforced one.
- Fiber grid reinforcement can slightly reduce the opening of internal cracks and so improve the fatigue crack resistance of reinforced structures. However, a high Young's modulus is required to observe significant effect. For a grid stiffness of 70 GPa the performance improvement is only 15%.
- Fiber grid reinforcement dramatically reduces the opening of surface-breaking cracks at the crack-surface intersection. This permits to contain the crack in its initial layer and prevent its propagation. The fatigue crack resistance of reinforced structures is thus significantly enhanced. Moreover, a high Young's modulus is not necessary to obtain good performance. Even for a stiffness of only

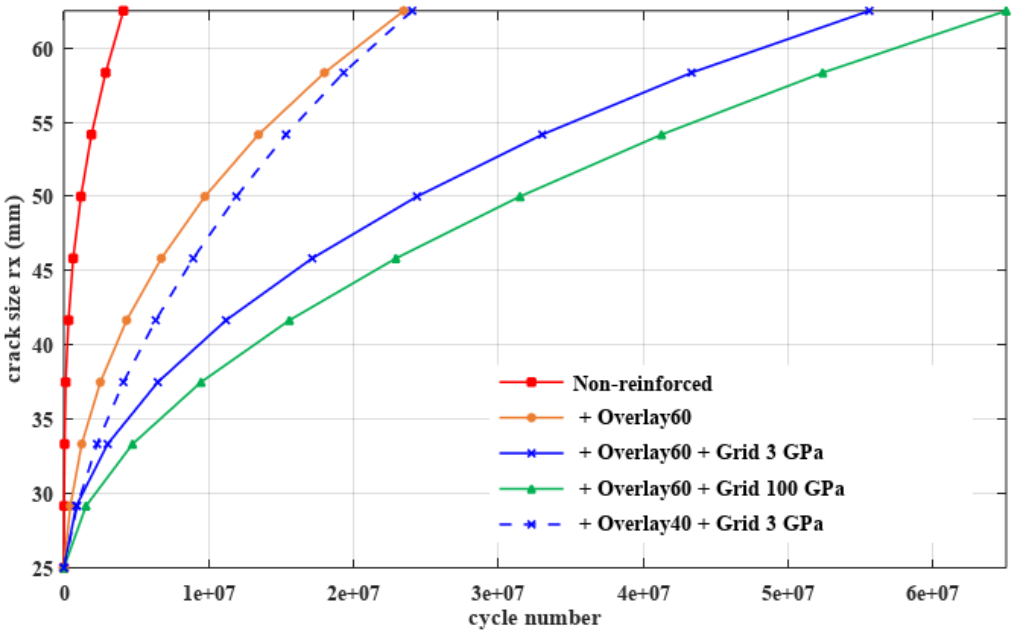

Figure 22. Cracking resistance in x direction considering a grid reinforcement on a cracked pavement (half of the norm of the complex modulus is used)

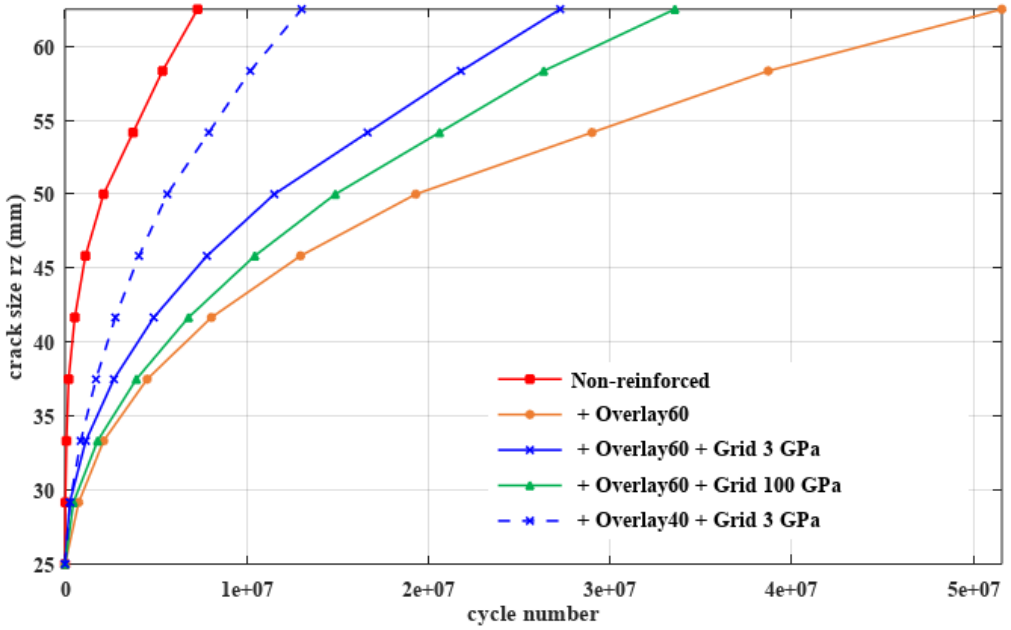

Figure 23. Cracking resistance in z direction considering a grid reinforcement on a cracked pavement (half of the norm of the complex modulus is used)

3 GPa, we obtained a fatigue performance improvement of a factor 2.2 due only to the addition of the fiber grid.

When we consider top – down propagation in reinforced pavement and neglect sliding and tangent stiffness for the grid bonding :

- Fatigue of surface breaking crack propagation: Fiber grid reinforcement strongly reduces the opening of surface-breaking cracks at the crack-surface intersection. This permits to decrease the crack propagation at the interface and prevent its propagation. The fatigue crack resistance of reinforced structures is thus significantly enhanced.
- In fatigue cracking resistance, the fiberglass grid ($E_g = 3\,\text{GPa}$) can replace 20mm to 30mm of asphalt concrete layer ($E = 11364\,\text{MPa}$) with the surface-breaking crack and the pavement structure considered in this study.
- Fatigue of crack propagation in the volume : For crack propagation in the volume of the layer, a stiff reinforcement improves also the mechanical behaviour in both directions but what has been observed is that in this case crack propagation is increased by the presence of the grid at the interface. This last result will be reconsidered with new propagation criterion and by taking into account propagation in the interface and through the reinforcement layer with down-top propagation.

In future work, imperfect interfaces will be introduced to model sliding or a tangent stiffness at the interface between the grid and pavement layers. More-elaborate propagation criteria will be investigated (propagation of the crack at the interface surface with branching and down-top propagation) and the influence of various factors (grid location, layer thickness, layer stiffness, etc.) on the performance of fiber grid reinforcement will be studied. Crack initiation will be investigated by computing the asymptotic response of an initiation criterion using a topological gradient approach.

Acknowledgements

This work was supported in part by the French National Research Agency (SolDuGri project ANR-14-CE22-0019) and in part by the Grand-Est region, France.

References

Abu-Farsakh, M. Y., Gu, J., Voyiadjis, G. Z., & Chen, Q. (2014). Mechanistic–empirical analysis of the results of finite element analysis on flexible pavement with geogrid base reinforcement. *International Journal of Pavement Engineering*, *15*(9), 786-798. Retrieved from `https://doi.org/10.1080/10298436.2014.893315`

Aliabadi, M. H., Rooke, D. P., & Cartwright, D. J. (1987). An improved boundary element formulation for calculating stress intensity factors: Application to aerospace structures. *The Journal of Strain Analysis for Engineering Design*, *22*(4), 203-207.

Arsenie, I. M., Chazallon, C., Duchez, J.-L., & Hornych, P. (2017). Laboratory characterisation of the fatigue behaviour of a glass fibre grid-reinforced asphalt concrete using 4pb tests. *Road Materials and Pavement Design*, *18*(1), 168-180. Retrieved from `https://doi.org/10.1080/14680629.2016.1163280`

Arsenie, I. M., Chazallon, C., Duchez, J.-L., & Mouhoubi, S. (2017). Modelling of the fatigue damage of a geogrid-reinforced asphalt concrete. *Road Materials and Pavement Design*, *18*(1), 250-262. Retrieved from `https://doi.org/10.1080/14680629.2016.1159973`

Bacchi, M. (2009). Evaluation of the effects of geo-composite reinforcement on fatigue life of asphalt pavements. In *Proceedings of the 2nd workshop on four-point bending. guimarães: University of minho.*

Baek, J., & Al-Qadi, I. (2009, 12). Reflective cracking: Modeling fracture behavior of hot-mix asphalt overlays with interlayer systems. *Asphalt Paving Technology: Association of Asphalt Paving Technologists-Proceedings of the Technical Sessions*, *78*, 789–827.

Barsoum, R. S. (1976). On the use of isoparametric finite element in linear fracture mechanics. *Int. J. Num. Meth. Eng.*, *10*, 25–37.

Belytschko, T., & Black, T. (1999). Elastic crack growth in finite elements with minimal remeshing. *International Journal for Numerical Methods in Engineering*, *45*(5), 601-620.

Belytschko, T., Liu, W., Moran, B., & Elkhodary, K. (2014). *Nonlinear finite elements for continua and structures*. John Wiley & Sons, Ltd.

Bondt, A. d., Schrader, J., Bijsterveld, W. v., & Long, D. (2005). *Scientific background of arcdeso-version april 2005* (Tech. Rep.). Internal Report-Ooms Nederland Holding.

Bonnet, M. (1999). *Boundary integral equation methods for solids and fluids*. John Wiley and sons.

Bouchard, P., Bay, F., & Chastel, Y. (2003). Numerical modelling of crack propagation: automatic remeshing and comparison of different criteria. *Computer Methods in Applied Mechanics and Engineering*, *192*(35), 3887 - 3908. Retrieved from `http://www.sciencedirect.com/science/article/pii/ S0045782503003918`

Brebbia, C., & Georgiou, P. (1979). Combination of boundary and finite elements in elastostatics. *Applied Mathematical Modelling*, *3*(3), 212 - 220. Retrieved from `http://www.sciencedirect.com/science/article/pii/0307904X79900532`

Canestrari, F., Belogi, L., Ferrotti, G., & Graziani, A. (2013, 09). Shear and flexural characterization of grid-reinforced asphalt pavements and relation with field distress evolution. *Materials and Structures*, *48*, 959–975.

Chen, Q., Hanandeh, S., Abu-Farsakh, M., & Mohammad, L. (2018). Performance evaluation of full-scale geosynthetic reinforced flexible pavement. *Geosynthetics International*, *25*(1), 26-36. Retrieved from `https://doi.org/10.1680/jgein.17.00031`

Coni, M., & Bianco, P. (2000). Steel reinforcement influence on the dynamic behaviour of bituminous pavement. In *Pro 11: 4th international rilem conference on reflective cracking in pavement research in practice* (Vol. 11, p. 6).

Costabel, M. (1987). Symmetric Methods for the Coupling of Finite Elements and Boundary Elements (Invited contribution). In C. A. Brebbia, W. L. Wendland, & G. Kuhn (Eds.), *Mathematical and Computational Aspects* (pp. 411–420). Berlin, Heidelberg: Springer Berlin Heidelberg.

Costabel, M., & Stephan, E. P. (1987, July). An improved boundary element Galerkin method for three-dimensional crack problems. *Integral Equations and Operator Theory*, *10*(4), 467–504. Retrieved from `https://doi.org/10.1007/BF01201149`

Costabel, M., & Stephan, E. P. (1990). Coupling of finite and boundary element methods for an elastoplastic interface problem. *SIAM Journal on Numerical Analysis*, *27*(5), 1212–1226.

Coulier, P., François, S., Lombaert, G., & Degrande, G. (2014). Coupled finite element – hierarchical boundary element methods for dynamic soil–structure interaction in the frequency domain. *International Journal for Numerical Methods in Engineering*, *97*(7), 505-530. Retrieved from `https://onlinelibrary.wiley.com/doi/abs/10.1002/nme.4597`

Dansou, A., Mouhoubi, S., & Chazallon, C. (2020, Aug). Optimizations of a fast multipole symmetric galerkin boundary element method code. *Numerical Algorithms*, *84*, 825 - 846. Retrieved from `https://doi.org/10.1007/s11075-019-00781-z`

Dansou, A., Mouhoubi, S., Chazallon, C., & Bonnet, M. (2019). Modeling multicrack propagation by the fast multipole symmetric galerkin bem. *Engineering Analysis with Boundary Elements*, *106*, 309 - 319. Retrieved from `http://www.sciencedirect.com/science/article/pii/ S0955799719302395`

Di Benedetto, H., & Corté, J.-F. (2004). *Matériaux routiers bitumineux: Constitution et propriétés thermomécaniques des mélanges*. Hermès science publications.

Erdogan, F., & Sih, G. C. (1963). On the crack extension in plates under plane loading and transverse shear. *J. Basic Eng.*, *85*, 519–525.

Frangi, A. (2002, August). Fracture propagation in 3D by the symmetric Galerkin boundary

element method. *International Journal of Fracture*, *116*(4), 313–330.

Fries, T.-P., & Belytschko, T. (2010). The extended/generalized finite element method: An overview of the method and its applications. *International Journal for Numerical Methods in Engineering*, *84*(3), 253-304.

Ganguly, S., Layton, J. B., & Balakrishna, C. (2000). Symmetric coupling of multi-zone curved Galerkin boundary elements with finite elements in elasticity. *International Journal for Numerical Methods in Engineering*, *48*(5), 633–654.

Greengard, L., & Rokhlin, V. (1987). A fast algorithm for particle simulations. *Journal of Computational Physics*, *73*(2), 325 - 348. Retrieved from `http://www.sciencedirect.com/science/article/pii/ 0021999187901409`

Gu, F., Luo, X., Luo, R., Hajj, E. Y., & Lytton, R. L. (2017). A mechanistic-empirical approach to quantify the influence of geogrid on the performance of flexible pavement structures. *Transportation Geotechnics*, *13*, 69 - 80. Retrieved from `http://www.sciencedirect.com/science/article/pii/ S2214391217300570` (SI:Pavement Geotechnics)

Gwinner, J., & Stephan, E. P. (2018). Fem-bem coupling. In *Advanced boundary element methods: Treatment of boundary value, transmission and contact problems* (pp. 451–536). Cham: Springer International Publishing.

Haas, M., Helldörfer, B., & Kuhn, G. (2006, Jun 09). Improved coupling of finite shell elements and 3D boundary elements. *Archive of Applied Mechanics*, *75*(10), 649. Retrieved from `https://doi.org/10.1007/s00419-006-0037-5`

Holek, M., & Fedeliński, P. (2020). Finite and boundary element analysis of crack closure. *Computer Methods in Materials Science*, *20*.

Hornych, P., Kerzrého, J.-P., Sohm, J., Chabot, A., Trichet, S., Joutang, J.-L., & Bastard, N. (2012). Full scale tests on grid reinforced flexible pavements on the french fatigue carrousel. In A. Scarpas, N. Kringos, I. Al-Qadi, & L. A. (Eds.), *7th rilem international conference on cracking in pavements* (pp. 1251–1260). Dordrecht: Springer Netherlands.

Khodaii, A., Fallah, S., & Moghadas Nejad, F. (2009). Effects of geosynthetics on reduction of reflection cracking in asphalt overlays. *Geotextiles and Geomembranes*, *27*(1), 1 - 8. Retrieved from `http://www.sciencedirect.com/science/article/pii/ S0266114408000381`

Le Fichoux, E. (2011). Présentation et utilisation de cast3m. *ENSTA-LME (http://www-cast3m.cea.fr)*.

Li, S., Mear, M., & Xiao, L. (1998). Symmetric weak-form integral equation method for three-dimensional fracture analysis. *Computer Methods in Applied Mechanics and Engineering*, *151*(3), 435 - 459. Retrieved from `http://www.sciencedirect.com/science/article/pii/ S0045782597001990` (Containing papers presented at the Symposium on Advances in Computational Mechanics)

Ma, S. (2005). *Propagation of the mixed mode crack in a welded specimen in elastic-plastic material*. Theses, Université Blaise Pascal - Clermont-Ferrand II. Retrieved from `https://tel.archives-ouvertes.fr/tel-00664816`

Margonari, M. (2004). *Boundary element techniques for three dimensional problems in elastostatics*. PhD Thesis, University of Trento.

Mi, Y., & Aliabadi, M. (1994). Three-dimensional crack growth simulation using bem. *Computers & Structures*, *52*(5), 871 - 878. Retrieved from `http://www.sciencedirect.com/science/article/pii/ 0045794994900728`

Millien, A., Dragomir, M. L., Wendling, L., Petit, C., & Iliescu, M. (2012). Geogrid interlayer performance in pavements: Tensile-bending test for crack propagation. In A. Scarpas, N. Kringos, I. Al-Qadi, & L. A. (Eds.), *7th rilem international conference on cracking in pavements* (pp. 1209–1218). Dordrecht: Springer Netherlands.

Moës, N., Dolbow, J., & Belytschko, T. (1999). A finite element method for crack growth without remeshing. *International Journal for Numerical Methods in Engineering*, *46*(1), 131-150.

Mouhoubi, S. (2000). *Symmetric FEM-BEM coupling in solid mechanics: formulation and*

implementation in a finite element code. PhD Thesis, Université de Limoges.

Nguyen, M.-L., Blanc, J., Kerzrého, J.-P., & Hornych, P. (2013). Review of glass fibre grid use for pavement reinforcement and apt experiments at ifsttar. *Road Materials and Pavement Design*, *14*(sup1), 287-308. Retrieved from https://doi.org/10.1080/14680629.2013.774763

Nguyen, M. L., Chupin, O., Blanc, J., Piau, J.-M., Hornych, P., & Lefeuvre, Y. (2020). Investigation of crack propagation in asphalt pavement based on apt result and lefm analysis. *Journal of Testing and Evaluation*, *48*(1), 161–177.

Nguyen, M. L., Hornych, P., Le, X. Q., Dauvergne, M., Lumiere, L., Chazallon, C., ... Godard, E. (2021). Development of a rational design procedure based on fatigue characterization and environmental evaluation of asphalt pavement reinforced with glass fibre grid. *EATA 2021, International Journal of Road Materials and Pavement design*.

Nguyen, T., Rungamornrat, J., Senjuntichai, T., & Wijeyewickrema, A. (2015). Fem-sgbem coupling for modeling of mode-i planar cracks in three-dimensional elastic media with residual surface tension effects. *Engineering Analysis with Boundary Elements*, *55*, 40 - 51. Retrieved from http://www.sciencedirect.com/science/article/pii/S0955799714002884 (Coupling Techniques)

Oliver, J., Huespe, A., & Sánchez, P. (2006). A comparative study on finite elements for capturing strong discontinuities: E-fem vs x-fem. *Computer Methods in Applied Mechanics and Engineering*, *195*(37), 4732 - 4752. Retrieved from http://www.sciencedirect.com/science/article/pii/ S0045782505005049 (John H. Argyris Memorial Issue. Part I)

Paris, P., & Erdogan, F. (1963). A critical analysis of crack propagation laws. *J. Basic Eng.*, *85*, 528–533.

Pham, A. D., Mouhoubi, S., Chazallon, C., & Bonnet, M. (2012). Fast multipole method applied to Symmetric Galerkin boundary element method for 3D elasticity and fracture problems. *Eng. Anal. Bound. Elem.*, *36*, 1838 – 1847.

Recho, N. (2013). Fracture mechanics. In *Fracture mechanics and crack growth* (p. 87-186). John Wiley & Sons, Ltd. Retrieved from https://onlinelibrary.wiley.com/doi/abs/10.1002/ 9781118387184.ch4

Safavizadeh, S. A., Wargo, A., Guddati, M., & Kim, Y. R. (2015). Investigating reflective cracking mechanisms in grid-reinforced asphalt specimens: Use of four-point bending notched beam fatigue tests and digital image correlation. *Transportation Research Record*, *2507*(1), 29-38. Retrieved from https://doi.org/10.3141/2507-04

Sagnol, L., Quezada, J. C., Chazallon, C., & Stockner, M. (2019). Effect of glass fibre grids on the bonding strength between two asphalt layers and its contact dynamics method modelling. *Road Materials and Pavement Design*, *20*(5), 1164-1181. Retrieved from https://doi.org/10.1080/14680629.2018.1439764

Springhetti, R., Novati, G., & Margonari, M. (2006). Weak coupling of the Symmetric Galerkin BEM with FEM for potential and elastostatic problems. *Computer Modeling in Engineering and Sciences*.

Sukumar, N., Chopp, D. L., Béchet, E., & Moës, N. (2008). Three-dimensional non-planar crack growth by a coupled extended finite element and fast marching method. *International Journal for Numerical Methods in Engineering*, *76*(5), 727-748. Retrieved from https://onlinelibrary.wiley.com/doi/abs/10.1002/nme.2344

Sun, C., & Jin, Z.-H. (2012). *Fracture Mechanics*. Academic Press.

Taherkhani, H., & Jalali, M. (2017). Investigating the performance of geosynthetic-reinforced asphaltic pavement under various axle loads using finite-element method. *Road Materials and Pavement Design*, *18*(5), 1200-1217. Retrieved from https://doi.org/10.1080/14680629.2016.1201525

Tam, A. B., Park, D.-W., Le, T. H. M., & Kim, J.-S. (2020). Evaluation on fatigue cracking resistance of fiber grid reinforced asphalt concrete with reflection cracking rate computation. *Construction and Building Materials*, *239*, 117873. Retrieved from

http://www.sciencedirect.com/science/article/pii/ S0950061819333264

Tang, X., Stoffels, S. M., & Palomino, A. M. (2016). Mechanistic-empirical approach to characterizing permanent deformation of reinforced soft soil subgrade. *Geotextiles and Geomembranes*, *44*(3), 429 - 441. Retrieved from http://www.sciencedirect.com/science/article/pii/ S026611441500062X

Thom, N. (2000). A simplified computer model for grid reinforced asphalt overlays. In *Proceedings of the 4th international rilem conference on reflective cracking in pavements* (pp. 37–46).

Trinh, Q. T., Mouhoubi, S., Chazallon, C., & Bonnet, M. (2015). Solving multizone and multicrack elastostatic problems: A fast multipole symmetric Galerkin boundary element method approach. *Eng. Anal. Bound. Elem.*, *50*, 486 – 495.

Vanelstraete, A., Leonard, D., & Veys, J. (2000). Structural design of roads with steel reinforcing nettings. In *Proceedings of the 4th int. rilem conf. cracking in pavements* (pp. 57–67).

von Estorff, O., & Hagen, C. (2005). Iterative coupling of FEM and BEM in 3D transient elastodynamics. *Engineering Analysis with Boundary Elements*, *29*(8), 775 - 787. Retrieved from http://www.sciencedirect.com/science/article/pii/S0955799705000998

Yoshida, K. (2001). *Applications of fast multipole method to boundary integral equation method.* PhD Thesis, Kyoto University.

Zienkiewicz, O. C., Kelly, D. W., & Bettess, P. (1977). The coupling of the finite element method and boundary solution procedures. *International Journal for Numerical Methods in Engineering*, *11*(2), 355-375. Retrieved from https://onlinelibrary.wiley.com/doi/abs/10.1002/nme.1620110210

Zofka, A., & Maliszewski, M. (2019). Practical overlay design method for geogrid reinforcement of asphalt layers. *Road Materials and Pavement Design*, *20*, S163–S182. Retrieved from https://doi.org/10.1080/14680629.2019.1590222 (Publisher: Taylor & Francis _eprint: https://doi.org/10.1080/14680629.2019.1590222)

Zofka, A., Maliszewski, M., & Maliszewska, D. (2017). Glass and carbon geogrid reinforcement of asphalt mixtures. *Road Materials and Pavement Design*, *18*, 471–490. Retrieved from https://doi.org/10.1080/14680629.2016.1266775 (Publisher: Taylor & Francis _eprint: https://doi.org/10.1080/14680629.2016.1266775)